HHS Public Access

Author manuscript

*Magn Reson Med*. Author manuscript; available in PMC 2021 January 01.

Published in final edited form as:

*Magn Reson Med*. 2020 January ; 83(1): 109–123. doi:10.1002/mrm.27914.

# Systematic Assessment of Multi-Echo Dynamic Susceptibility Contrast (DSC) MRI using a Digital Reference Object (DRO)

**Ashley M. Stokes, PhD**[*], **Natenael B. Semmineh, PhD**, **Ashley Nespodzany, MS**, **Laura C. Bell, PhD**, **C. Chad Quarles, PhD**

Division of Neuroimaging Research, Barrow Neurological Institute, Phoenix AZ 85013, USA

## Abstract

**Purpose:** Brain tumor dynamic susceptibility contrast (DSC) MRI is adversely impacted by $T_1$ and $T_2$* contrast agent leakage effects that result in inaccurate hemodynamic metrics. While multi-echo acquisitions remove $T_1$ leakage effects, there is no consensus on the optimal set of acquisition parameters. Using a computational approach, we systematically evaluated a wide range of acquisition strategies to determine the optimal multi-echo DSC-MRI perfusion protocol.

**Methods:** Using a population-based DSC-MRI digital reference object (DRO), we assessed the influence of preload dosing (no preload and full dose preload), field strength (1.5 and 3T), pulse sequence parameters (echo time (TE), repetition time (TR), and flip angle (FA)), and leakage correction on relative cerebral blood volume (rCBV) and flow (rCBF) accuracy. We also compared multi-echo DSC-MRI protocols to standard single-echo protocols.

**Results:** Multi-echo DSC-MRI is highly consistent across all protocols, and multi-echo rCBV (with or without use of a preload dose) had higher accuracy than single-echo rCBV. Regression analysis showed that choice of TR and FA had minimal impact on multi-echo rCBV and rCBV, indicating the potential for significant flexibility in acquisition parameters. The TE combination had minimal impact on rCBV, though longer TEs should be avoided, particularly at higher field strengths. Leakage correction improved rCBV accuracy in all cases. Multi-echo rCBF was less biased than single-echo rCBF, although rCBF accuracy was reduced overall relative to rCBV.

**Conclusions:** Multi-echo acquisitions were more robust than single-echo, essentially decoupling both TR and FA from rCBV accuracy. Multi-echo acquisitions obviate the need for preload dosing, though leakage correction to remove residual $T_2$* leakage effects remains compulsory for high rCBV accuracy.

### Keywords

perfusion; dynamic susceptibility contrast (DSC); digital reference object (DRO); brain tumor hemodynamics; multi-echo

[*]Corresponding author: Ashley M. Stokes, Division of Neuroimaging Research, Barrow Neurological Institute, 350 W. Thomas Rd, Phoenix Arizona 85013, USA, ashley.stokes@barrowneuro.org, (602) 406-8789.

## Introduction

Dynamic susceptibility contrast MRI (DSC-MRI) can be used to inform upon hemodynamic characteristics in the brain, including cerebral blood volume (CBV). In brain tumors, relative CBV (rCBV) relates to tumor angiogenesis, making it a valuable biomarker for diagnosis and treatment in neuro-oncology (1–3). One challenge for DSC-MRI in brain tumors is contrast agent leakage through the blood-brain barrier (BBB), which is often degraded due to the abnormal tumor neovasculature. Contrast agent leakage, which manifests as simultaneous $T_1$ and $T_2$* effects, ultimately limits the reliability of rCBV measurements (2,4). $T_1$ leakage effects lead to rCBV underestimation, while $T_2$* leakage effects typically lead to rCBV overestimation. Standard DSC-MRI protocols have varying sensitivities to $T_1$ and $T_2$*, which further complicates the expected impact on rCBV. Advanced pulse sequences that acquire multiple echoes (5–7) may provide an additional advantage because $T_1$ leakage effects can be removed, thus potentially providing more robust rCBV measures (4).

Many strategies have been proposed to minimize the effects of contrast agent leakage. On the acquisition side, both contrast agent dosing and pulse sequence parameters can have an impact on the relative contribution of leakage effects. Contrast agent pre-load dosing reduces $T_1$ leakage effects, while sequence parameters (echo time (TE), repetition time (TR), and flip angle (FA)) can be modified to optimize the relative weighting of $T_2$* effects over $T_1$ effects (8). Despite these efforts to optimize preload dosing and acquisition protocols, leakage correction remains essential in brain tumors (9). The most commonly applied leakage correction method - termed Boxerman-Schmainda-Weisskoff (BSW) - leverages non-enhancing reference tissue to estimate leakage effects, which can then be subtracted from the leakage-affected tumor tissue (2,10). One challenge for leakage correction methods is that they must simultaneously correct for both $T_1$ and $T_2$* leakage effects, which have dissimilar underlying biophysical bases. Using multi-echo protocols, only $T_2$* leakage effects must be accounted for during leakage correction (4).

Many recent efforts have aimed at standardizing acquisition and analysis protocols for DSC-MRI, where the recommendations are largely based on clinical performance (9). This is largely due to the challenges associated with dynamic bolus imaging, where repeat imaging with varying protocols is impractical (note that even if injection dose was not a concern, contrast agent leakage effects would vary across bolus doses). A computational approach using a digital reference object (DRO) can overcome these challenges by permitting the assessment of a wide array of protocols. Using a validated, population-based DRO (11), rCBV accuracy was previously assessed across more than 6000 single-echo protocols (12). The DRO-driven recommendation for clinical trials was a full-dose preload, followed by a full dose bolus, with 60° FA, 30 ms TE at 3T (50 ms at 1.5T), 1.5s TR, and use of leakage correction. This protocol effectively minimizes $T_1$ leakage effects, while optimizing the $T_2$* contrast. Unfortunately, there is no consensus on the optimal multi-echo DSC-MRI protocol (13), which is increasingly available for perfusion imaging and may provide a more comprehensive hemodynamic assessment. The purpose of this study is to systematically evaluate a wide range of acquisition strategies using a DSC-DRO to determine the optimal multi-echo perfusion protocol.

## Methods:

### $T_1$ and $T_2$* pulse sequence sensitivity:

DSC-MRI signal is simultaneously sensitive to both $T_1$ and $T_2$* effects, and the relative contribution of $T_1$ and $T_2$* is modulated by the pulse sequence parameters (TE, TR, and FA). The signal is given by Equation 1:

$$S = \frac{S_0 \sin(\alpha) e^{-TE \cdot R_2^*} (1 - e^{-TR \cdot R_1})}{1 - \cos(\alpha) e^{-TR \cdot R_1}} \quad [1]$$

where $S_0$ is the equilibrium magnetization, α is FA, and $R_2$* (=1/$T_2$*) and $R_1$ (=1/$T_1$) are the transverse and longitudinal relaxivities, respectively. The single-echo signal sensitivity to $T_1$ and $T_2$* can be derived from Equation 1:

$$\frac{\partial S}{\partial R_2^*} = -TE \cdot S = -TE \cdot \frac{S_0 \sin(\alpha) e^{-TE \cdot R_2^*} (1 - e^{-TR \cdot R_1})}{1 - \cos(\alpha) e^{-TR \cdot R_1}} \quad [2]$$

$$\frac{\partial S}{\partial R_1} = \frac{S_0 \sin(\alpha) e^{-TE R_2^*} (TR \cdot e^{-TR \cdot R_1} - \cos(\alpha) \cdot TR \cdot e^{-TR \cdot R_1})}{(1 - \cos(\alpha) e^{-TR \cdot R_1})^2} \quad [3]$$

When multiple echoes are acquired with a given TR and FA, each signal has the same $R_1$ contribution but a different amount of $R_2$*. By combining echoes, the $R_1$ contribution can be removed:

$$S_{ME} = \frac{S_1}{S_2} = e^{-(TE_2 - TE_1) \cdot R_2^*} \quad [4]$$

Thus, the sensitivity of the multi-echo signal to $R_1$ is null, while the sensitivity to $T_2$* effects depends on the difference between TE1 and TE2:

$$\frac{\partial S_{ME}}{\partial R_2^*} = -(TE_2 - TE_1) \cdot e^{-(TE_2 - TE_1) \cdot R_2^*} \quad [5]$$

Multi-echo acquisitions also permit extrapolation of the signal to TE = 0, which contains only $R_1$ effects and excludes $R_2$* effects. The sensitivity of the multi-echo $T_1$-weighted signal can be assessed from Equation 3, where TE = 0.

### Construction of digital reference object (DRO):

While these signal equations provide insight into $T_1$ and $T_2$* sensitivity, they are not sufficient to assess the effects of contrast agent passing through biological tissue, due to the complex relationship between susceptibility effects and vascular and cellular architecture (14–16). This necessitates the use of computational methods to model susceptibility-induced field perturbations arising from complex tissue topographies. In this work, a population-based DRO was used to systematically assess and optimize multi-echo DSC-MRI perfusion protocols. The details of the DRO were published previously for validation (11) and single-echo protocol optimization (12). Briefly, the DRO calculates the MR signal from realistic 3D tissue structures, with the cells and vessels simulated as ellipsoids packed around randomly oriented cylinders, respectively. A pharmacokinetic two-compartmental model (17) was used to compute the vascular and extravascular contrast agent concentration time-courses using physiologically relevant CBV, cerebral blood flow (CBF), volume transfer constants ($K^{trans}$), and extravascular-extracellular volume fractions ($v_e$). A population-based arterial input function (AIF) from the training dataset was used as the input for kinetic modeling. The resulting concentration time-courses were combined with the simulated tissue structures, water diffusion coefficient, and relevant pulse sequence parameters to compute $\Delta R_2$* time curves using the finite perturber finite difference method (FPFDM) (14). To ensure clinical relevance, the DRO was trained and validated using two distinct datasets from glioblastoma patients (11). The distribution of CBV and CBF was determined using a training dataset of 23 subjects with a mean (range) CBV and CBF of 6.1% (1.5–13.8) and 150.3 ml/100g/min (43.9–268.2), respectively, while $K^{trans}$ varied between 0.03 and 0.47 (mean 0.19) (11). The average mean transit time (MTT) was 6.9 s (standard deviation = 3.5) in tumor, compared to 5.7 s (standard deviation = 1.5) in white matter. Gaussian noise was added to match the contrast-to-noise (CNR) from the in vivo training data set. The DRO was validated using a separate dataset, where the same structural and kinetic inputs obtained during the training phase were used but with different acquisition parameters, contrast agent, and contrast agent dose. The DRO accurately recapitulated the signals from this separate validation dataset, thus indicating that the trained DRO can accurately model various pulse sequence parameters and dosing schemes. A range of DROs are available for download from both The Cancer Imaging Archive (www.cancerimagingarchive.net) in Digital Imaging and Communications in Medicine (DICOM) format and from the Quantitative Imaging Biomarker Alliance (QIBA, http://qibadscdro.rsna.org). The specific DROs used in this study are also available upon request.

### In Silico MRI Methods:

DRO MRI data were simulated at both 1.5T and 3T. The MRI protocol included three flip angles (30, 60, and 90) and three repetition times (TRs, 1, 1.5, and 2 s). To test the optimal combination of echo times, seven echo times were simulated (2, 5, 20, 30, 40, 60, and 70 ms). Two minutes of MRI data were simulated for each parameter combination, with the injection occurring after 60 seconds. Two injection protocols were simulated: no preload with single-dose bolus (0+1) and single-dose preload and bolus (1+1). For each parameter combination, the DRO produced 10,000 voxels with varying CA leakage effects. A parallel set of 10,000 voxels was simulated without leakage ($K^{trans} = 0$) for each parameter

combination. A smaller subset of normal appearing white matter voxels (2,000) were also simulated for each parameter combination.

### Post-processing and Data Analysis:

Each echo time was assessed individually (single-echo) and in pair-wise combinations, for a total of 21 multi-echo (specifically, dual-echo) combinations. For single-echo and multi-echo combinations, $\Delta R_2^*$ was calculated using Equations [6] and [7], respectively.

$$\Delta R_2^* = \frac{-\ln\left(S(t)/S(0)\right)}{TE} \quad [6]$$

$$\Delta R_{2,ME}^* = \frac{-1}{(TE_2 - TE_1)}\left(\ln\left(\frac{S_{TE1}(t)}{S_{TE1}(0)}\right) - \ln\left(\frac{S_{TE2}(t)}{S_{TE2}(0)}\right)\right) \quad [7]$$

where *S(0)* denotes the pre-bolus (baseline) signal. It should be noted that Equation [6] is derived from Equation [1] by assuming that the $T_1$ contribution is negligible. For multi-echo combinations, the $T_1$ contributions are explicitly removed (Equation [7]). In addition to the single- and dual-echo combinations, a multi-echo log-linear fit to all echoes was also assessed. For consistency, all dual-echo combinations and the multi-echo fit will be henceforth referred to as multi-echo combinations; where relevant, the results from the multi-echo fit will be specified in the text. Leakage correction was performed on both the single-echo and multi-echo data using the standard BSW method (2,18), modified to account for both positive ($T_1$) and negative ($T_2^*$) leakage effects (19). Relative CBV (rCBV) was determined by integration of the $\Delta R_2^*$ curve over two minutes (60 s of baseline), followed by normalization to the normal-appearing white matter voxels. While this integration likely included some recirculation components, gamma-variate fitting was not used in this study (discussed in further detail below). Tumor rCBV was compared to the rCBV expected in the absence of contrast agent leakage ($K^{trans} = 0$). CBF was determined from the maximum of the impulse response function obtained from circular singular value decomposition (cSVD) of the input AIF with the tissue $\Delta R_2^*$, using a fixed threshold of 0.10 (20). CBF was then normalized to normal-appearing white matter, yielding rCBF. The total number of combinations tested were 2088 (29 TE possibilities, 3 TRs, 3 FA, 2 dosing strategies, 2 field strengths, and with and without leakage correction). Comparisons between estimated and expected perfusion parameters (rCBV and rCBF) were performed voxel-wise; comparisons across acquisition parameters (TE, TR, FA, etc.) were performed using the mean value across all 10,000 simulated tumor voxels for each parameter combination.

### Statistical Analysis:

Statistical analyses were performed using SPSS software (IBM SPSS Statistics for Windows, Version 19, Armonk, NY). Estimated rCBV was compared to the expected ($K^{trans} = 0$) rCBV across all parameter combinations. Percent rCBV differences ((estimated–expected)/expected) were compared across eight groups (separated by single- and multi-

echo, with and without preload, and uncorrected and BSW corrected), where negative values indicate rCBV underestimation and positive values indicate rCBV overestimation. A one-way analysis of variance (ANOVA) was used to compare across these groups. A secondary ANOVA was performed, excluding both no-preload, single-echo combinations, due to high variance and limited clinical applicability. Post-hoc analyses were performed using the Bonferroni method to adjust for multiple comparisons. Regression analysis was conducted to determine which parameters (FA, TR, TE (single-echo only), TE separation (multi-echo only), field strength, inclusion of preload, and correction algorithm) contributed to rCBV and rCBF accuracy for single-echo and multi-echo DSC-MRI. Concordance correlation coefficient (CCC) and coefficient of variation (CV) were used to assess linear agreement and relative variability, respectively, for each parameter combination. The accuracy and precision (AP) index, defined as CCC – |CV|, was used to determine the optimal parameter combinations. Results were considered significant at $p < 0.05$.

## Results:

The signal sensitivity to $T_2$* effects, as a function of tissue $T_2$*, can be calculated from Equations [2] (single-echo) and [5] (multi-echo) and is shown in Figure 1 for a range of pulse sequence combinations. The top panel (a, b) represents what would be achieved with a typical multi-echo EPI-based sequence (2 echoes, TEs = 20 and 40ms). The middle panel (c, d) represents a spiral-based acquisition, based on a spiral-out / spiral-out trajectory (TEs = 2 and 30ms) (21). Finally, the bottom panel (e, f) represents an extreme with two very short TEs, which may be achievable using single-line methods (albeit with much shorter TRs, which are not represented here). The multi-echo $T_2$* sensitivity (black curve) is decoupled from both TR and FA and exceeds that of the single-echo signal sensitivity (red and blue curves) in almost all cases (Eq. 2). Single-echo $T_2$* sensitivity varies as a function of tissue $T_2$*, TE, TR, and FA, while multi-echo $T_2$* sensitivity increases as a function of tissue $T_2$* and TE separation.

Multi-echo $\Delta R_2$* time-courses are insensitive to $T_1$ effects, while single-echo $\Delta R_2$* time-courses reflect a combination of $T_1$ and $T_2$* effects. The relative impact of $T_1$ effects can be calculated from Equation [3] (for both single- and multi-echo) and can be seen in Figure 2 as a function of TE, TR, and FA. $T_1$ effects vary as a function of tissue $T_2$* and can be minimized using longer TE, lower FA, and longer TR. Using a multi-echo acquisition, the $T_1$ sensitivity is isolated in the extrapolated TE=0 signal, while $T_2$* sensitivity is maintained in the $\Delta R_2$* partition. Similar to single-echo, higher $T_1$ sensitivity for the multi-echo TE=0 signal is observed for higher FA and lower TR. The TE combination does not impact the relative $T_1$ sensitivity, nor does the tissue $T_2$*. Moreover, the $T_1$ sensitivity for multi-echo TE=0 exceeds that of both input TEs.

Figure 3 demonstrates the impact of pulse sequence parameters and dosing on DSC-DRO $\Delta R_2$* time-courses after BSW correction (colored curves) and without leakage (black curves). The multi-echo $\Delta R_2$* (a-c, e-g) is highly consistent across all parameters and doses. Despite leakage correction, the peak $\Delta R_2$* is underestimated for all parameter combinations, while the post-bolus $\Delta R_2$* is overestimated compared to the no leakage curves (solid black lines). The TE combination and choice of preload dose have minimal impact on the multi-

echo $\Delta R_2$* (a-c, e-g), most notably on the peak $\Delta R_2$*. TR and FA have no effect on the multi-echo $\Delta R_2$*; conversely, TR and FA have a sizable impact on single-echo $\Delta R_2$* (d, h), particularly for the no preload case (d). In addition, the multi-echo fit (c, g) appears qualitatively similar to both two-echo combinations (a, b, e, f).

Scatter plots between the expected (no leakage) and estimated (BSW-corrected) rCBV for single-echo (TE = 30ms, red) and multi-echo (TE = 2 and 30ms, blue) are shown in Figure 4 for multiple combinations (no preload (lighter color) and with preload (darker color), 1 and 2s TR, 30 and 90 FA, and 1.5 and 3T field strength). Multi-echo rCBV is highly consistent across dosing protocols, TRs, FAs, and field strengths. In addition, multi-echo rCBV shows high agreement with the expected rCBV, which is also apparent in the Bland-Altman plots (Supporting Information Figure S1). Single-echo protocols that include a preload have higher agreement than protocols without a preload. In particular, single-echo protocols with high FA and short TR suffer from poor agreement in the absence of a preload; consistent with Figure 2, these protocols emphasize $T_1$ effects at the expense of $T_2$* sensitivity. Higher agreement is also observed at the higher field strength for single-echo rCBV, likely due to increased $T_2$* effects at higher field strengths.

Figure 5 demonstrates the rCBV percent difference between the estimated and expected rCBV across all 2088 parameter combinations. Each single-echo column accounts for 126 combinations (7 TEs, 3 TRs, 3 FAs, and 2 field strengths); each multi-echo column accounts for 396 combinations (22 TE combinations, 3 TRs, 3 FAs, and 2 field strengths). Across columns, the mean rCBV percent difference (as indicated by the blue x) is as follows: −1650, −517, −13.8, −12.8% for single-echo columns and 22.64, −1.5, 21.7, and 0.8% for multi-echo columns. In all cases, the inclusion of leakage correction substantially improves rCBV accuracy. For single-echo protocols, the inclusion of a preload also improves rCBV accuracy, while preload dosing does not improve the accuracy for multi-echo protocols. The single-echo estimated rCBV that did not include a preload was significantly different from the expected rCBV, even following leakage correction ($p < 0.001$, **). After exclusion of the no-preload, single-echo rCBV, across the six remaining combinations, four combinations were significantly different from expected (0% difference, $p < 0.001$, ++), where the corrected multi-echo rCBV were not significantly different (both with and without preload). As the multi-echo column in Figure 5 includes all two-echo combinations (21 combinations) and the log-linear fit, a further comparison was performed between the two-echo combinations and the multi-echo fit (Supporting Information Figure S3). The rCBV percent difference for the multi-echo fit was similar to the two-echo combinations, particularly following leakage correction. In addition, the use of a multi-echo fit did not improve rCBV accuracy over the two-echo combinations.

Multiple regression analysis revealed that all parameters, except field strength ($p = 0.180$), were significant predictors for single-echo rCBV estimates (all $p < 0.001$, except where indicated): FA, TR ($p = 0.03$), TE, inclusion of preload, and correction algorithm. In contrast, TR, FA, and TE separation were not significant predictors for multi-echo rCBV estimates ($p = 0.364$, 0.864, and 0.595, respectively), while field strength, preload, and inclusion of correction were significant ($p < 0.001$ for field strength and correction, $p = 0.021$ for preload).

The CV and CCC across all parameter combinations for each field strength are shown in Figure 6. At 1.5T (a, c), the CV approaches 0 and CCC approaches 1 with a tight distribution across all multi-echo combinations, regardless of the presence of a preload dose. At 3T (b, d), the vast majority of multi-echo combinations have low CV and high CCC, although there are some combinations that result in low agreement (specifically combinations with two long TEs, such as 60 and 70ms). While there are single-echo combinations that have high CCC and low CV across both field strengths, they are not as ubiquitous as for multi-echo. Even in the presence of a preload, many single-echo protocols demonstrate high CV and low CCC.

Figure 7 shows the combined AP index across 896 parameter combinations (1.5s TR and 60 FA were excluded for brevity). High rCBV accuracy can be obtained at both 1.5T and 3T (left vs. right), and leakage correction improves rCBV accuracy (top vs. bottom) across parameter space. For each TR and FA combination, the lower diagonal represents no preload, while the upper diagonal represents a single-dose preload. Single-echo rCBV (along each diagonal) tends to be inaccurate without preload, particularly with higher FA, due to predominant $T_1$ leakage effects. TR and FA have minimal impact on multi-echo rCBV accuracy, consistent with multiple regression analysis detailed above ($p = 0.364$ and 0.864 for TR and FA, respectively). In the absence of leakage correction, use of a preload reduces multi-echo rCBV accuracy, most likely due to additional $T_2$* leakage effects. Leakage correction adequately corrects for these $T_2$* leakage effects. Finally, the TE combination has minimal impact on multi-echo rCBV accuracy, although long TE combinations (both TEs ≥ 60ms) are detrimental at 3T. Across field strengths, TRs, FAs, and TE combinations, multi-echo DSC with leakage correction provides highly accurate rCBV values, as indicated by near-unity AP index values.

The top-performing acquisition parameter combinations for both single-echo and multi-echo DSC for each field strength and dosing scheme are shown in Table 1. For single-echo DSC, the optimal parameters reflect the need to minimize $T_1$ effects (long TR and low FA) and emphasize $T_2$* effects (long TE, particularly at 1.5T). For multi-echo DSC, the top-performing combination has a short TR, reflecting the lack of $T_1$ sensitivity in multi-echo DSC, and the multi-echo AP values match or exceed those of the top-performing single-echo AP values. To further highlight the flexibility of multi-echo acquisitions, the median AP values are shown for both single-echo and multi-echo rCBV. In the absence of a preload, the median AP index for single-echo drops to 0.25 at 1.5T and 0.54 at 3T, while preloads improve the median AP index. On the other hand, the median multi-echo AP index ranges from 0.87 to 0.91 across preloads and field strengths. There are hundreds of highly accurate protocols available with multi-echo DSC, while few are available for single-echo acquisitions, particularly in the absence of a preload.

The accuracy of rCBF may also be modulated by pulse sequence parameters, dosing strategies, and contrast agent leakage effects. Figure 8 illustrates the scatter plots between the expected (no leakage) and estimated (BSW-corrected) rCBF for single-echo (TE = 30ms) and multi-echo (TE = 2 and 30ms) DSC-MRI. The bottom row (i-l) shows the scatter plots for uncorrected rCBF at 3T. For both multi- and single-echo protocols, the estimated rCBF is underestimated (negative bias) relative to the expected rCBF, which is also apparent from the

Bland-Altman plots (Figure S2) in the Supporting Information. For multi-echo rCBF, higher agreement and less bias is observed relative to single-echo rCBF (AP index range = 0.80–0.84 (multi-echo, no preload) and 0.75–0.81 (multi-echo, with preload) vs. −0.14–0.79 (single-echo, no preload) and 0.55–0.80 (single-echo, with preload)). For single-echo rCBF, higher flip angles reduce the agreement, particularly in the absence of a preload, indicating that rCBF may also be sensitive to $T_1$ leakage effects. However, leakage correction does not have a substantial impact on the estimated rCBF (e-h vs. i-l). Across all combinations, including both multi-echo and single-echo, there is a trend of increasingly underestimated rCBF as rCBF increases, which is also apparent in the Bland-Altman plots (Supporting Information Figure S2).

Figure 9 shows the combined AP index for rCBF across 896 parameter combinations. Higher rCBF AP index values can be obtained at 1.5T than 3T (left vs. right), where the TE combinations that include longer TEs have less accurate rCBF. In contrast to rCBV, leakage correction does not impact rCBF accuracy (top vs. bottom). The inclusion of preloads (upper diagonal) slightly decreases rCBF accuracy for multi-echo protocols, while single-echo protocols have better rCBF accuracy in the presence of a preload. A similar trend to rCBV, with higher FA yielding lower accuracy, was also observed for single-echo rCBF. All parameters, except for field strength, were predictive of single-echo rCBF AP index ($p < 0.001$ for all, $p = 0.103$ for field strength). TR and FA have no discernible impact on multi-echo rCBF AP index ($p = 0.439$ and 0.291, respectively), and in contrast to rCBV, leakage correction did not impact rCBF AP index ($p = 0.175$). Field strength, dose, and TE separation were all significant predictors for rCBF AP index ($p < 0.001$). Across field strengths, TRs, and FAs, with moderate TE combinations, multi-echo DSC provides more accurate rCBF values, as indicated by higher AP index values.

## Discussion:

Standardized protocols for DSC-MRI have the potential to provide more robust and consistent rCBV measurements, enhancing its utility in both routine patient management and in the context of clinical trials. There are unique challenges for assessing DSC-MRI protocols in patients across parameter space because of the need for a bolus injection, as well as a lack of validated biophysical phantoms. This has led to a DRO-based optimization paradigm, where thousands of protocols can be assessed using validated tissue structures. Prior work using the DSC-DRO has focused on optimizing single-echo protocols, which must carefully balance $T_1$ and $T_2$* effects (12). In this work, we have shown that multi-echo DSC-MRI protocols may overcome nearly all of the challenges associated with single-echo DSC-MRI protocol standardization. Multi-echo DSC-MRI essentially decouples TR and FA from rCBV accuracy, leading to a wide range of pulse sequence options that yield robust rCBV. However, it is important to note that some TR and FA combinations outside of the range tested herein may have reduced accuracy even with multi-echo protocols; for example, long TRs may not accurately sample bolus passage, and very small FAs would reduce signal intensity. Pre-load dosing is often considered compulsory in single-echo DSC-MRI, but we have demonstrated that multi-echo DSC-MRI does not benefit from pre-load dosing. The implications of these results are that contrast agent dosing can be significantly reduced using

multi-echo acquisitions, while also providing pulse sequence flexibility in terms of TR and FA.

Contrast agent leakage is known to adversely impact rCBV metrics, while rCBF is thought to be minimally impacted by leakage effects (4,22). The purpose of a preload dose is to minimize $T_1$ leakage effects, which lead to underestimated rCBV. Based on the variability of results for single-echo protocols in the presence of a preload dose, we can infer that preload dosing does not completely mitigate $T_1$ effects. With strong leakage effects and no preload, leakage correction is typically unable to adequately compensate for these effects. One exception is protocols that inherently minimize $T_1$ effects, such as lower flip angle and longer TR and TE protocols. The relatively high performance of low flip angles protocols matches the previously published DSC-DRO (12) and has been further validated in vivo (23). A drawback to this no-preload low flip angle approach is that shorter TRs and lower field strength reduces its rCBV accuracy; in addition, there may be signal-to-noise ratio (SNR) and CNR penalties associated with reduced flip angle acquisitions (8). In contrast, multi-echo protocols enable $T_1$ leakage effects to be removed and are not sensitive to TR and FA, offering robust alternatives to single-echo protocols.

For most single-echo protocols with a preload and all multi-echo protocols with and without a preload, $T_2$* leakage effects lead to overestimation of rCBV. Close inspection of the $\Delta R_2$* curves in Figure 3 demonstrate that contrast agent leakage modulates the dynamic curves in a way that is not adequately compensated for by leakage correction. More specifically, the peak $\Delta R_2$* is underestimated, while the post-bolus $\Delta R_2$* is overestimated, relative to the no leakage curves shown in black. This would suggest that short integration limits may underestimate CBV, while longer integration limits would overestimate CBV. Previous DSC-DRO results found that 60 seconds of post-bolus integration is optimal (12), which is likely a good balance to cancel $\Delta R_2$* peak overestimation and post-bolus underestimation. For rCBV, leakage correction improves accuracy and appears to adequately correct $T_2$* leakage effects. However, almost no improvement was observed for rCBF with leakage correction, which highlights the sensitivity of CBF to the shape of the curves (as CBF is assessed with deconvolution, as opposed to integration for CBV). The trends observed in rCBF (as well as the lower peak corrected $\Delta R_2$* values) likely arise from inability of the BSW correction to account for the time- and concentration-dependent reduction in the susceptibility difference between the intra- and extravascular space (4,24,25) due to the initial leakage of contrast agent. Future work may focus on improving CBF accuracy using alternative methods of leakage correction (4,26,27).

Based on the signal sensitivity to $T_2$*, one would expect that combinations with short TE separation would yield reduced accuracy, while combinations that include wider TE separation would have increased rCBV accuracy. The shortest TE combination (2 and 5 ms) shows low rCBV accuracy at 1.5T, while the results are stronger at 3T, reflecting the higher $T_2$* effects at 3T. Regardless, leakage correction yields high AP index values, despite the small TE difference. In contrast, the TE combination that includes the two longest TEs (60 and 70 ms) has reduced AP index values at 3T, even with leakage correction. In practice, long TE combinations are ill-advised at higher field strengths due to concerns about signal saturation (28). Clearly, $T_2$* sensitivity is not the sole driver of rCBV accuracy; rather, the

rCBV accuracy as a function of TE combination is also impacted by image SNR. The SNR from multi-echo acquisitions is bounded by the longest TE (29). As TE1 varies from 2 to 60 ms, with TE2 = 70 ms, AP index decreases with decreasing TE separation, as expected from $T_2$* sensitivity alone. However, for TE1 = 2 ms and TE2 = 5–70 ms, the AP index is parabolic: it increases initially with increasing ΔTE, but then decreases as TE2 approaches 70 ms. One possible explanation is that despite the large TE separation, the AP index decreases due to the competing SNR penalty associated with the longer TE. Most intermediate combinations provide high rCBV accuracy, including combinations achievable with both EPI and spiral readouts (TEs = 20, 40 ms and 2, 30 ms, respectively).

Several previous studies have shown the advantages of multi-echo fits in vivo relative to two-echo combinations (30–32). In particular, some studies have shown improved SNR, particularly in regions with large susceptibility effects (such as near air-tissue interfaces), and have suggested more accurate $T_2$* quantification using multiple echoes (30,32). However, another study showed no net gain in SNR using multi-echo fits (31). Consistent with that study, no overt advantage was observed using a multi-echo fit relative to two-echo combinations. However, one possible explanation is that the DRO does not represent non-ideal in vivo tissue, in that the intrinsic $T_2$* is fairly homogeneous (that is, regions of high susceptibility are not explicitly considered). In addition, the use of a log-linear fit is known to give greater weights to low intensity data (such as the longer TEs), which may have biased the multi-echo fit in this study. This effect can be mitigated by either a weighted least-squares fit (31) or by fitting directly to the mono-exponential model (32). However, a previous study showed improved results using a log-linear fit over a mono-exponential fit, which the authors attributed to greater fit stability (32). Future work with both the single- and multi-echo DRO will assess how increasing noise impacts the resulting hemodynamic metrics, which may be more generally applicable to in vivo DSC-MRI.

Multi-echo protocols have many clear advantages for DSC-MRI, including acquisition flexibility and obsolescence of preload dosing. The former will enable widespread protocol adherence, while the latter will reduce total contrast agent dose, which is timely given recent concerns about gadolinium deposition in the brain (33). While the inclusion of longer echoes may result in compromises between spatial and temporal resolution, it should be noted that the inclusion of shorter echo times (relative to the standard recommendations of 30ms at 3T and 40ms at 1.5T (9)) does not typically impact pulse sequence parameters that influence spatial and temporal resolution, given the so-called dead space between the excitation pulse and the standard echo time. Multi-echo protocols may also provide additional advantages that have not been considered directly herein. Although the removal of $T_1$ effects is advantageous for DSC-MRI, the remaining $T_1$-weighted signal (TE = 0) can be leveraged for simultaneous dynamic contrast enhanced (DCE-) MRI (7,21,22,34–36). Previous studies have demonstrated excellent agreement between dual-echo DSC- and standard DCE-derived pharmacokinetic parameters (specifically $K^{trans}$ and $v_e$) (6). Based on Figure 2, multi-echo protocols may provide enhanced $T_1$ sensitivity, while lacking sensitivity to competing $T_2$* effects that may be a potential source of bias (37). This multi-echo DRO may provide novel insight into these advantages in the future.

Another potential advantage for multi-echo protocols is for quantifying the AIF, which is critical for deconvolution to obtain CBF. Previous studies have shown that the AIF is adversely impacted by concurrent $T_1$ effects, which can substantially reduce the resulting CBF measures (up to 40%) (38). In addition, the optimal TE for measuring the AIF was previously estimated to be 12 ms, which is far shorter than both the typical DSC-MRI protocol and the reported optimal tumor TE (30 ms) (39). Multi-echo sequences may permit the optimization of individual echoes for AIF and tissue, particularly when at least one TE is less than 15 ms. Finally, the correlation between individual echoes in multi-echo protocols may serve as a unique criterion to improve automated AIF selection (40).

While the DRO developed for this study was trained and validated against a cohort of glioblastoma patients, some of the conclusions can be extended to other brain tumor types. Specifically, primary central nervous system lymphomas are known to have strong $T_1$ leakage effects, while brain tumor metastases have stronger $T_2$* leakage effects (41). In the case of lymphomas, multi-echo sequences would likely provide higher rCBV accuracy than single-echo protocols due to the insensitivity to $T_1$ leakage effects. However, for metastatic brain tumors, it is possible that the stronger $T_2$* leakage effects could lead to a different set of optimal parameters, most likely with shorter TEs. Additional DROs have been developed to study different brain tumor types, with vascular and cellular features consistent with the known histopathological characteristics of these tumor types (42). Work is currently underway to more broadly characterize DSC-based hemodynamic metrics across these brain tumor types.

There are several important limitations for this study. In contrast to the single-echo DSC-DRO optimization study, we did not assess the impact of different leakage correction algorithms or rCBV limits of integration. One notable drawback of the BSW correction is its known sensitivity to the reference tissue MTT (4,26), which was not considered here. As most leakage models are based on contrast agent kinetics, we expect other models to have similar accuracy to the BSW correction, while more advanced leakage correction algorithms that include a biophysical component may provide more robust hemodynamic metrics (4,26). Regarding integration limits, the single-echo DRO optimization study showed that 11 of the top 12 parameter combinations utilized integration of two minutes of data (60s pre-injection and 60s post-injection), which is consistent with the integration limits in the current study. In theory, integration should occur only over the first-pass to minimize the effects of recirculation (43), though previous studies proposed 120-point integration (TR = 1s) as a standard limit with good results (8). Gamma-variate fitting has also been proposed to reduce the impact of recirculation, but this was not used in this study due to the previously observed low accuracy (12) and known potential to introduce errors (44). Finally, there are some limitations regarding our quantification of rCBF. The AIF used in this study was the simulation tissue input function, and thus we did not account for diffusion or the altered biophysics of the AIF (although pulse sequence parameters were accounted for in each AIF). However, we do not expect the AIF shape or magnitude to change drastically upon consideration of the unique biophysics (including larger vessel diameter, higher vascular volume fraction, higher flow velocities, and fewer vascular bifurcations). In addition, the tissue structures comprising the DRO may not be physiologically representative of the capillary bed. A fixed regularization threshold of 10% was used in this study, which was

previously shown to provide the highest agreement with expectations for circular SVD (20). However, alternative approaches may include the use of an oscillation index (45), L-curve criterion (20,46), or SNR-dependent thresholds (47). Further investigation into optimal deconvolution approaches for multi-echo DSC-MRI is outside of the scope of this paper and may be the focus of future work.

## Conclusions:

In conclusion, multi-echo acquisitions are more robust than single-echo acquisitions, essentially decoupling both TR and FA from rCBV accuracy. Multi-echo rCBV is more consistent and had higher AP index values (indicating higher accuracy and lower variance) than the single-echo options, indicating the potential for significant flexibility in acquisition parameters. Multi-echo acquisitions do not benefit from a preload injection, which may obviate many of the associated drawbacks with preload dosing. With multi-echo acquisitions, the TE combination has minimal impact on rCBV, and inclusion of a shorter multi-echo TE slightly improves AP index. At 1.5T, rCBF accuracy did not depend on TE combination, while moderate TE combinations provided higher rCBF accuracy at 3T. Leakage correction improves rCBV accuracy in all cases but did not impact rCBF. In addition, lower rCBF accuracy was observed compared to rCBV accuracy, particularly at higher field strengths. Multi-echo DSC-MRI provides a highly robust perfusion protocol for brain tumor imaging that could also improve intra- and inter-site consistency, rendering it a compelling option for use in patient management and in clinical trials.

## Supplementary Material

Refer to Web version on PubMed Central for supplementary material.

## Acknowledgements:

This work was supported by the Arizona Biomedical Research Commission (ADHS16–162414) and NIH/NCI R01CA213158–01.

**Funding Sources:** This work was supported by the Arizona Biomedical Research Commission (ADHS16–162414) and NIH/NCI R01CA213158–01.

## References:

1. Hu LS, Eschbacher JM, Heiserman JE, et al. Reevaluating the imaging definition of tumor progression: perfusion MRI quantifies recurrent glioblastoma tumor fraction, pseudoprogression, and radiation necrosis to predict survival. Neuro Oncol [Internet] 2012;14:919–930. doi: 10.1093/neuonc/nos112.
2. Boxerman JL, Schmainda KM, Weisskoff RM. Relative cerebral blood volume maps corrected for contrast agent extravasation significantly correlate with glioma tumor grade, whereas uncorrected maps do not. AJNR Am J Neuroradiol [Internet] 2006;27:859–867.
3. Schmainda KM, Prah M, Connelly J, Rand SD, Hoffman RG, Mueller W, Malkin MG. Dynamic-susceptibility contrast agent MRI measures of relative cerebral blood volume predict response to bevacizumab in recurrent high-grade glioma. Neuro. Oncol 2014;16:880–888. doi: 10.1093/neuonc/not216. [PubMed: 24431219]
4. Stokes AM, Semmineh N, Quarles CC. Validation of a T1 and T2* leakage correction method based on multiecho dynamic susceptibility contrast MRI using MION as a reference standard. Magn. Reson. Med. [Internet] 2016;76:613–625. doi: 10.1002/mrm.25906.

5. Vonken EPA, van Osch MJP, Bakker CJG, Viergever MA. Simultaneous quantitative cerebral perfusion and Gd-DTPA extravasation measurement with dual-echo dynamic susceptibility contrast MRI. Magn. Reson. Med. [Internet] 2000;43:820–827. doi: 10.1002/1522-2594(200006)43:6<820::AID-MRM7>3.0.CO;2-F.
6. Quarles CC, Gore JC, Xu L, Yankeelov TE. Comparison of dual-echo DSC-MRI- and DCE-MRI-derived contrast agent kinetic parameters. Magn. Reson. Imaging [Internet] 2012;30:944–953. doi: 10.1016/j.mri.2012.03.008.
7. Stokes AM, Skinner JT, Quarles CC. Assessment of a combined spin- and gradient-echo (SAGE) DSC-MRI method for preclinical neuroimaging. Magn. Reson. Imaging [Internet] 2014;32:1181–1190. doi: 10.1016/j.mri.2014.08.027.
8. Paulson ES, Schmainda KM. Comparison of Dynamic Susceptibility-weighted Contrast-enhanced MR Methods: Recommendations for Measuring Relative Cerebral Blood Volume in Brain Tumors. Radiology [Internet] 2008;249:601–613. doi: doi:10.1148/radiol.2492071659.
9. Welker K, Boxerman J, Kalnin A, Kaufmann T, Shiroishi M, Wintermark M, American Society of Functional Neuroradiology MRPS, Practice Subcommittee of the ACPC. ASFNR recommendations for clinical performance of MR dynamic susceptibility contrast perfusion imaging of the brain. AJNR Am J Neuroradiol [Internet] 2015;36:E41–51. doi: 10.3174/ajnr.A4341.
10. Boxerman JL, Prah DE, Paulson ES, Machan JT, Bedekar D, Schmainda KM. The Role of preload and leakage correction in gadolinium-based cerebral blood volume estimation determined by comparison with MION as a criterion standard. AJNR Am J Neuroradiol [Internet] 2012;33:1081–1087. doi: 10.3174/ajnr.A2934.
11. Semmineh NB, Stokes AM, Bell LC, Boxerman JL, Quarles CC. A Population-Based Digital Reference Object (DRO) for Optimizing Dynamic Susceptibility Contrast (DSC)-MRI Methods for Clinical Trials. Tomography [Internet] 2017;3:41–49. doi: 10.18383/j.tom.2016.00286.
12. Semmineh NB, Bell LC, Stokes AM, Hu LS, Boxerman JL, Quarles CC. Optimization of Acquisition and Analysis Methods for Clinical Dynamic Susceptibility Contrast MRI Using a Population-Based Digital Reference Object. Am. J. Neuroradiol. [Internet] 2018. doi: 10.3174/ajnr.A5827.
13. Stokes AM, Semmineh NB, Quarles CC. Systematic Assessment of Multi-Echo Dynamic Susceptibility Contrast (DSC) MRI using a Digital Reference Object (DRO). In: Proceedings of the 26th Annual Meeting of ISMRM.; 2018 p. 2188.
14. Semmineh NB, Xu J, Boxerman JL, Delaney GW, Cleary PW, Gore JC, Quarles CC. An efficient computational approach to characterize DSC-MRI signals arising from three-dimensional heterogeneous tissue structures. PLoS One [Internet] 2014;9:e84764. doi: 10.1371/journal.pone.0084764.
15. Pathak AP, Ward BD, Schmainda KM. A novel technique for modeling susceptibility-based contrast mechanisms for arbitrary microvascular geometries: the finite perturber method. Neuroimage [Internet] 2008;40:1130–1143. doi: 10.1016/j.neuroimage.2008.01.022.
16. Boxerman JL, Hamberg LM, Rosen BR, Weisskoff RM. MR contrast due to intravascular magnetic susceptibility perturbations. Magn. Reson. Med. [Internet] 1995;34:555–566. doi: 10.1002/mrm.1910340412.
17. Brix G, Bahner ML, Hoffmann U, Horvath A, Schreiber W. Regional Blood Flow, Capillary Permeability, and Compartmental Volumes: Measurement with Dynamic CT—Initial Experience. Radiology [Internet] 1999;210:269–276. doi: doi:10.1148/radiology.210.1.r99ja46269.
18. Weisskoff RM, Boxerman JL, Sorensen AG, Kulke SM, Campbell TA, Rosen BR. Simultaneous blood volume and permeability mapping using a single Gd-based contrast injection. In: Proceedings of the 2nd Annual Meeting of SMRM. San Francisco, CA, USA; 1994 p. 279.
19. Liu H-L, Wu Y-Y, Yang W-S, Chen C-F, Lim K-E, Hsu Y-Y. Is Weisskoff model valid for the correction of contrast agent extravasation with combined T[sub 1] and T[sub 2]∗] effects in dynamic susceptibility contrast MRI? Med. Phys 2011;38:802. doi: 10.1118/1.3534197. [PubMed: 21452717]
20. Bjørnerud A, Emblem KE. A fully automated method for quantitative cerebral hemodynamic analysis using DSC – MRI. J. Cereb. Blood Flow Metab 2010;30:1066–1078. doi: 10.1038/jcbfm.2010.4. [PubMed: 20087370]

21. Paulson ES, Prah DE, Schmainda KM. Spiral Perfusion Imaging With Consecutive Echoes (SPICE) for the Simultaneous Mapping of DSC- and DCE-MRI Parameters in Brain Tumor Patients: Theory and Initial Feasibility. Tomography [Internet] 2016;2:295–307. doi: 10.18383/j.tom.2016.00217.
22. Vonken E, van Osch M, Bakker C, Viergever M. Simultaneous quantitative cerebral perfusion and Gd-DTPA extravasation measurement with dual-echo dynamic susceptibility contrast MRI. Magn. Reson. Med. [Internet] 2000;43:820–827.
23. Schmainda KM, Prah MA, Hu LS, et al. Moving Toward a Consensus DSC-MRI Protocol: Validation of a Low – Flip Angle Single-Dose Option as a Reference Standard for Brain Tumors. AJNR. Am. J. Neuroradiol 2019:626–633. [PubMed: 30923088]
24. Sourbron S, Heilmann M, Walczak C, Vautier J, Schad LR, Volk A. T2*-relaxivity contrast imaging: first results. Magn. Reson. Med. [Internet] 2013;69:1430–1437. doi: 10.1002/mrm.24383.
25. Semmineh NB, Xu J, Skinner JT, Xie J, Li H, Ayers G, Quarles CC. Assessing tumor cytoarchitecture using multiecho DSC-MRI derived measures of the transverse relaxivity at tracer equilibrium (TRATE). Magn. Reson. Med. [Internet] 2014. doi: 10.1002/mrm.25435.
26. Bjornerud A, Sorensen AG, Mouridsen K, Emblem KE. T1- and T2*-dominant extravasation correction in DSC-MRI: part I--theoretical considerations and implications for assessment of tumor hemodynamic properties. J Cereb Blood Flow Metab [Internet] 2011;31:2041–2053. doi: 10.1038/jcbfm.2011.52.
27. Leu K, Boxerman JL, Cloughesy TF, Lai A, Nghiemphu PL, Liau LM, Pope WB, Ellingson BM. Improved Leakage Correction for Single-Echo Dynamic Susceptibility Contrast Perfusion MRI Estimates of Relative Cerebral Blood Volume in High-Grade Gliomas by Accounting for Bidirectional Contrast Agent Exchange. Am. J. Neuroradiol. [Internet] 2016;37:1440 LP–1446. doi: 10.3174/ajnr.A4759.
28. Thilmann O, Larsson EM, Bjorkman-Burtscher IM, Stahlberg F, Wirestam R. Effects of echo time variation on perfusion assessment using dynamic susceptibility contrast MR imaging at 3 tesla. Magn. Reson. Imaging [Internet] 2004;22:929–935. doi: 10.1016/j.mri.2004.01.079.
29. Glover GH, Lemieux SK, Drangova M, Pauly JM. Decomposition of inflow and blood oxygen level-dependent (BOLD) effects with dual-echo spiral gradient-recalled echo (GRE) fMRI. Magn. Reson. Med. [Internet] 1996;35:299–308. doi: 10.1002/mrm.1910350306.
30. Newbould RD, Skare ST, Jochimsen TH, Alley MT, Moseley ME, Albers GW, Bammer R. Perfusion mapping with multiecho multishot parallel imaging EPI. Magn. Reson. Med. [Internet] 2007;58:70–81. doi: 10.1002/mrm.21255.
31. Jochimsen TH, Newbould RD, Skare ST, Clayton DB, Albers GW, Moseley ME, Bammer R. Identifying systematic errors in quantitative dynamic-susceptibility contrast perfusion imaging by high-resolution multi-echo parallel EPI. Nmr Biomed. [Internet] 2007;20:429–438. doi: 10.1002/nbm.1107.
32. Hietschold V, Abramyuk A, Juratli T, Sitoci-Ficici KH, Laniado M, Linn J. Magnetic Resonance Perfusion in Brain Tumors: Comparison of Different Evaluation Approaches in Dual-Echo and Multi-Echo Techniques. Int. J. Med. Physics, Clin. Eng. Radiat. Oncol 2017;06:174–192. doi: 10.4236/ijmpcero.2017.62016.
33. McDonald RJ, McDonald JS, Kallmes DF, Jentoft ME, Murray DL, Thielen KR, Williamson EE, Eckel LJ. Intracranial Gadolinium Deposition after Contrast-enhanced MR Imaging. Radiology [Internet] 2015;275:772–782. doi: 10.1148/radiol.15150025.
34. Barbier EL, den Boer JA, Peters AR, Rozeboom AR, Sau J, Bonmartin A. A model of the dual effect of gadopentetate dimeglumine on dynamic brain MR images. J. Magn. Reson. Imaging [Internet] 1999;10:242–253. doi: 10.1002/(SICI)1522-2586(199909)10:3<242::AID-JMRI4>3.0.CO;2-H.
35. Schmiedeskamp H, Andre JB, Straka M, Christen T, Nagpal S, Recht L, Thomas RP, Zaharchuk G, Bammer R. Simultaneous perfusion and permeability measurements using combined spin- and gradient-echo MRI. J Cereb Blood Flow Metab [Internet] 2013;33:732–743. doi: 10.1038/jcbfm.2013.10.
36. Skinner JT, Moots PL, Ayers GD, Quarles CC. On the Use of DSC-MRI for Measuring Vascular Permeability. AJNR Am J Neuroradiol [Internet] 2016;37:80–87. doi: 10.3174/ajnr.A4478.

37. Ewing JR, Bagher-Ebadian H. Model selection in measures of vascular parameters using dynamic contrast-enhanced MRI: Experimental and clinical applications. NMR Biomed 2013;26:1028–1041. doi: 10.1002/nbm.2996. [PubMed: 23881857]
38. Calamante F, Vonken EJ, van Osch MJ. Contrast agent concentration measurements affecting quantification of bolus-tracking perfusion MRI. Magn. Reson. Med. [Internet] 2007;58:544–553. doi: 10.1002/mrm.21362.
39. Bell LC, Does MD, Stokes AM, Baxter LC, Schmainda KM, Dueck AC, Quarles CC. Optimization of DSC MRI Echo Times for CBV Measurements Using Error Analysis in a Pilot Study of High-Grade Gliomas. AJNR Am J Neuroradiol [Internet] 2017;38:1710–1715. doi: 10.3174/ajnr.A5295.
40. Newton AT, Skinner JT, Quarles CC. Automatic AIF Estimation in Multi-Echo DSC-MRI of Pediatric Patients - Avoiding the Noise Floor. In: Proceedings of the 21st Annual Meeting of ISMRM. Salt Lake City, UT, USA; 2013 p. 3064.
41. Mangla R, Kolar B, Zhu T, Zhong J, Almast J, Ekholm S. Percentage signal recovery derived from MR dynamic susceptibility contrast imaging is useful to differentiate common enhancing malignant lesions of the brain. AJNR Am J Neuroradiol [Internet] 2011;32:1004–1010. doi: 10.3174/ajnr.A2441.
42. Semmineh NB, Bell LC, Stokes AM, Mathew E, Lee M, Boxerman JL, Quarles CC. Investigating the Influence of DSC-MRI Acquisition Methods on the Clinical Application of Percentage Signal Recovery in Brain Tumors. In: Proceedings of the 27th Annual Meeting of ISMRM.; 2019 p. 392.
43. Kiselev VG. On the theoretical basis of perfusion measurements by dynamic susceptibility contrast MRI. Magn. Reson. Med 2001;46:1113–1122. doi: 10.1002/mrm.1307. [PubMed: 11746577]
44. Willats L, Calamante F. The 39 steps: evading error and deciphering the secrets for accurate dynamic susceptibility contrast MRI. Nmr Biomed. [Internet] 2013;26:913–931. doi: 10.1002/nbm.2833.
45. Wu O, stergaard L, Weisskoff RM, Benner T, Rosen BR, Sorensen AG. Tracer arrival timing-insensitive technique for estimating flow in MR perfusion-weighted imaging using singular value decomposition with a block-circulant deconvolution matrix. Magn. Reson. Med. [Internet] 2003;50:164–174.
46. Calamante F, Gadian DG, Connelly A. Quantification of bolus-tracking MRI: Improved characterization of the tissue residue function using Tikhonov regularization. Magn. Reson. Med. [Internet] 2003;50:1237–1247. doi: 10.1002/mrm.10643.
47. Liu H-L, Pu Y, Liu Y, Nickerson L, Andrews T, Fox PT, Gao J-H. Cerebral blood flow measurement by dynamic contrast MRI using singular value decomposition with an adaptive threshold. Magn. Reson. Med. [Internet] 1999;42:167–172. doi: 10.1002/(SICI)1522-2594(199907)42:1<167::AID-MRM22>3.0.CO;2-Q.

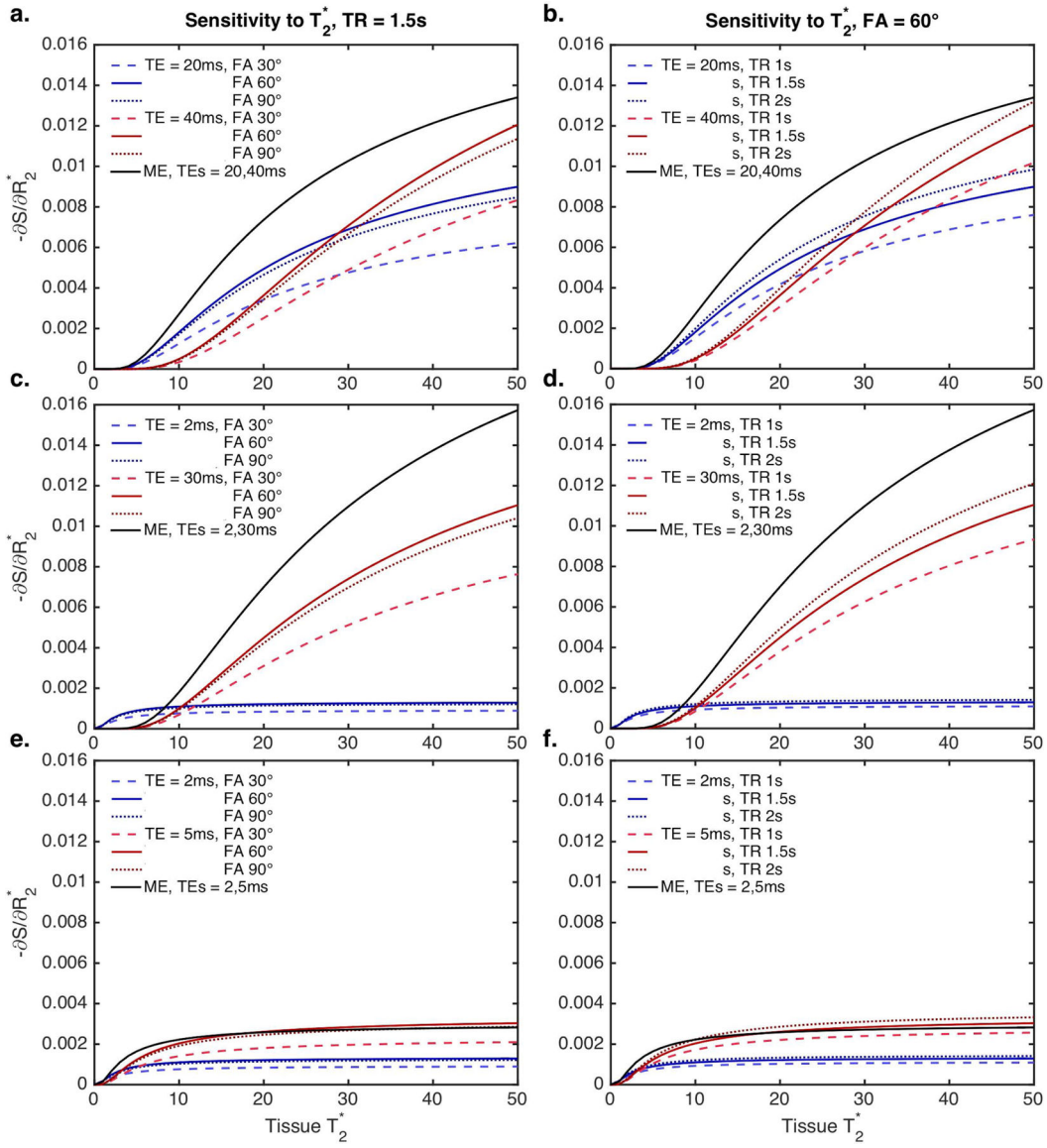


**Figure 1.**

Signal sensitivity to $T_2$* effects, as a function of tissue $T_2$*, for a range of pulse sequence combinations (left: TR = 1.5s, FA = 30, 60, and 90º; right: FA = 60º, TR = 1, 1.5, and 2 s). a, b: TEs = 20 and 40 ms (representative of a typical dual-echo EPI-based sequence); c, d: TEs = 2 and 30 ms (representative of a spiral-based acquisition); e, f: TEs = 2 and 4ms. The multi-echo $T_2$* sensitivity is shown in black (no variation for TR and FA), while the single-echo $T_2$* sensitivity is shown in red and blue (with TR and FA variations).

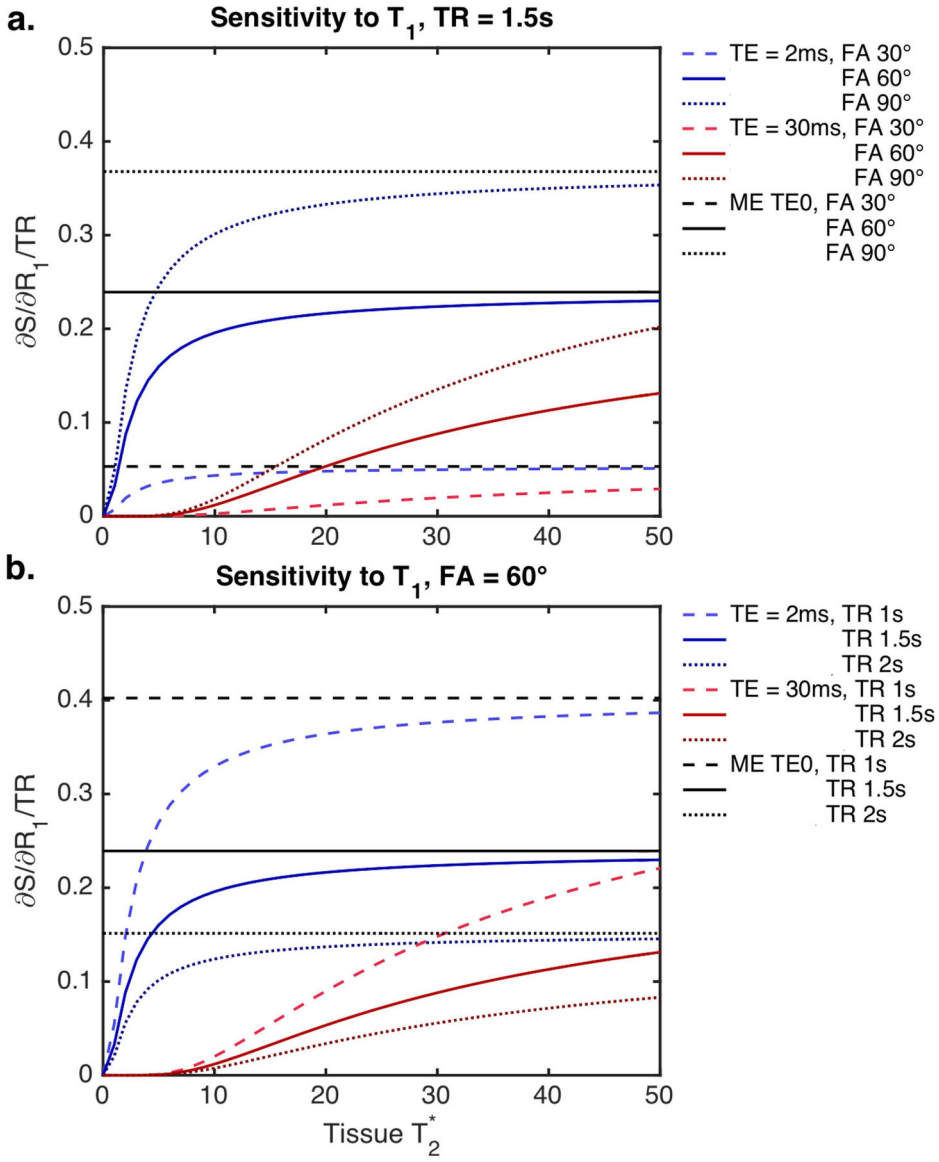


**Figure 2.**

Signal sensitivity to T1 effects, as a function of tissue $T_2$*, for a range of pulse sequence combinations (a: TR = 1.5s, FA = 30, 60, and 90º; b: FA = 60º, TR = 1, 1.5, and 2 s). Multi-echo TE = 0 (black) and single-echo protocols (red and blue) vary with TR and FA. Single-echo protocols must balance T1 and $T_2$* sensitivity, whereas multi-echo protocols separate these effects. For multi-echo protocols, the TE combination and tissue $T_2$* do not impact the relative T1 sensitivity.

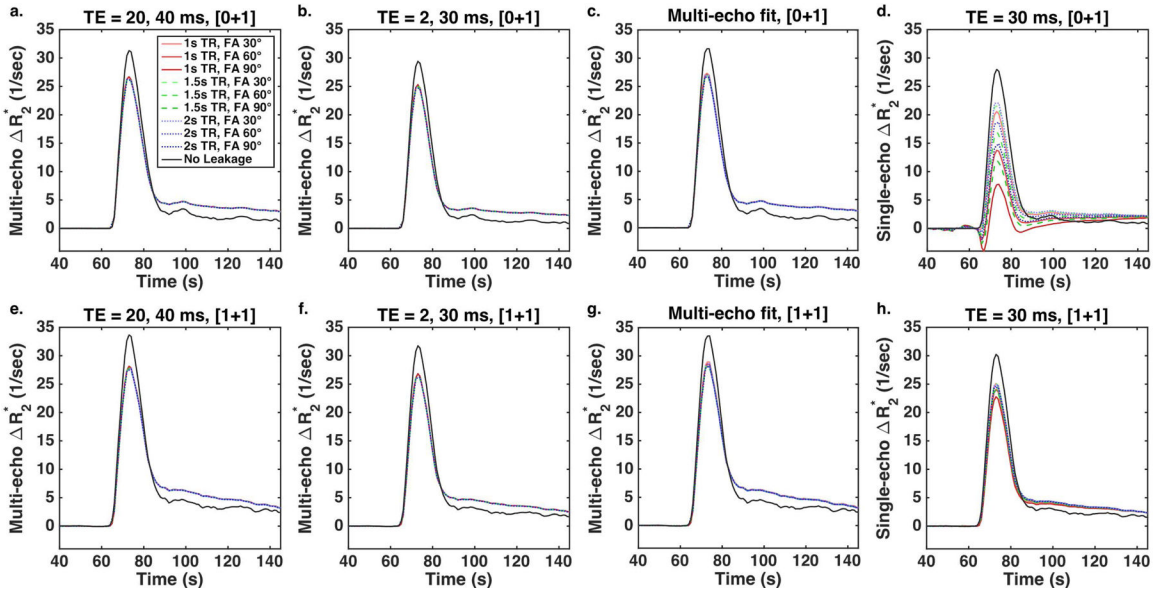


**Figure 3.**

DSC-DRO $\Delta R_2^*$ time-courses after BSW correction (colored curves) and without leakage (black curves) across TR (1 (red), 1.5 (green), and 2 (blue) s) and FA (30, 60, and 90º, light to dark shades) without a preload (a-d) and with a full dose preload (e-h). The multi-echo $\Delta R_2^*$ (a, e: TEs = 20, 40 ms; b, f: TEs = 2, 30 ms, c, g: multi-echo fit) is highly consistent across parameters and doses, although leakage correction does not fully compensate for the leakage effects. TR and FA have a sizable impact on single-echo $\Delta R_2^*$ (d, h: TE = 30 ms), particularly in the absence of a preload.

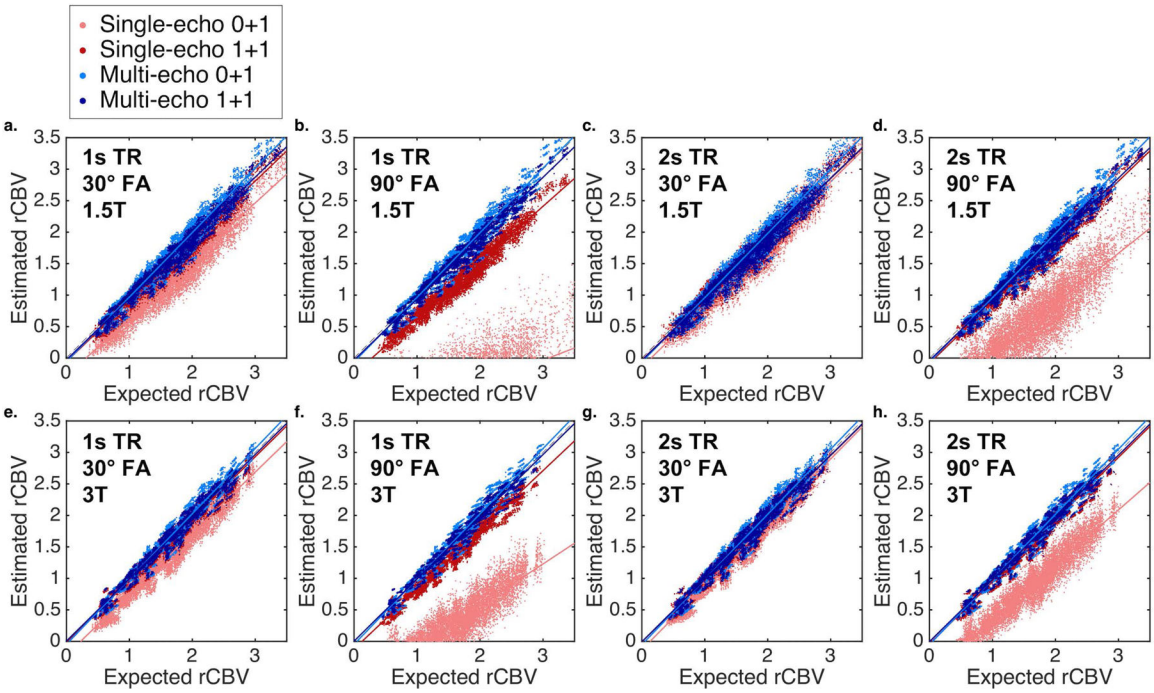


**Figure 4.**

Scatter plots between the expected (no leakage) and estimated (BSW-corrected) rCBV for single-echo (TE = 30ms, red) and multi-echo (TE = 2 and 30ms, blue) with no preload (light color) and with preload (dark color) for TR and FA combinations (a, e: 1s TR and 30º FA; b, f: 1s TR and 90º FA; c, g: 2s TR and 30º FA; d, h: 2s TR and 90º FA;) at 1.5 (a-d) and 3T (e-h). Solid lines indicate best-fit lines, while the black dashed lines indicate the line of unity.

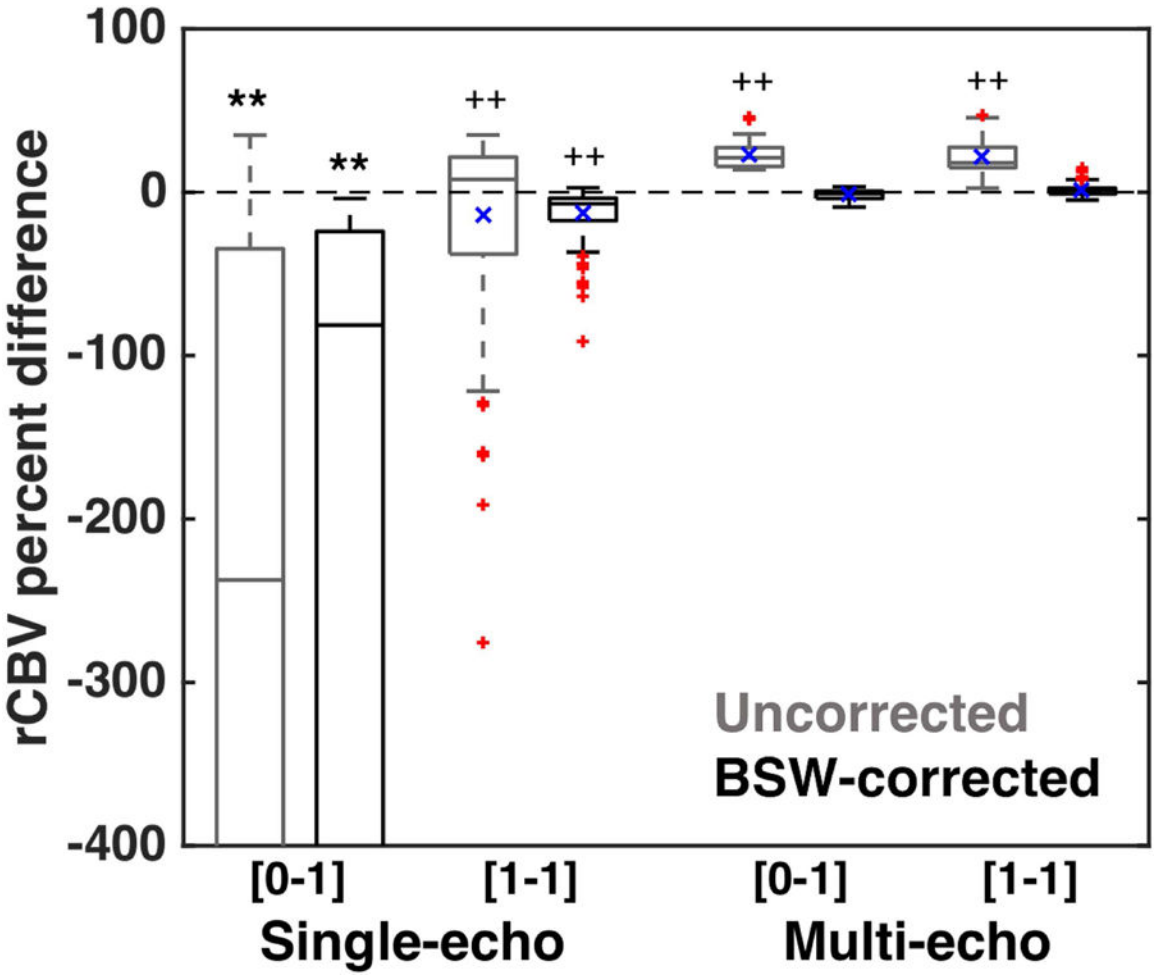


**Figure 5.**

rCBV percent difference between the estimated and expected rCBV for single-echo (126 combinations) and multi-echo (396 combinations) parameter combinations. Single-echo rCBV without a preload was significantly different from the expected rCBV, even with leakage correction ($p < 0.001$, **). Secondary analysis revealed that only corrected multi-echo rCBV was not significantly different from 0 (all others: $p < 0.001$, ++), across all dosing strategies, field strengths, TRs, FAs, and TE combinations. Significant differences from preliminary ANOVA are indicated by ** ($p < 0.001$) and secondary ANOVA are indicated by ++ ($p < 0.001$). The horizontal bar in each boxplot indicates median values, while the blue x indicates mean values. The mean values for each column can also be found in the text.

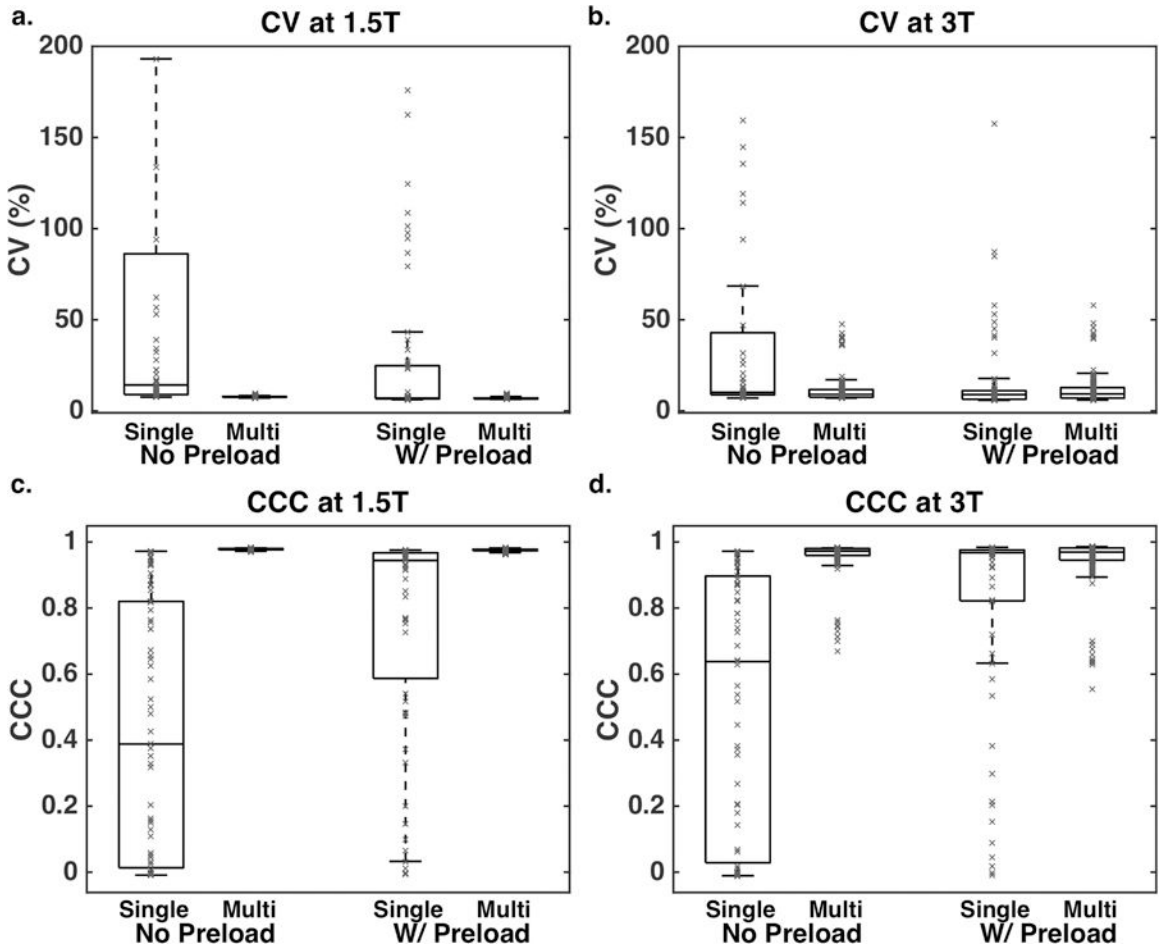


**Figure 6.**

CV (a, b) and CCC (c, d) across all parameter combinations for each field strength (a, c: 1.5T, b, d: 3T). A tighter distribution, with lower CV and higher CCC, is observed for multi-echo protocols compared to single-echo protocols.

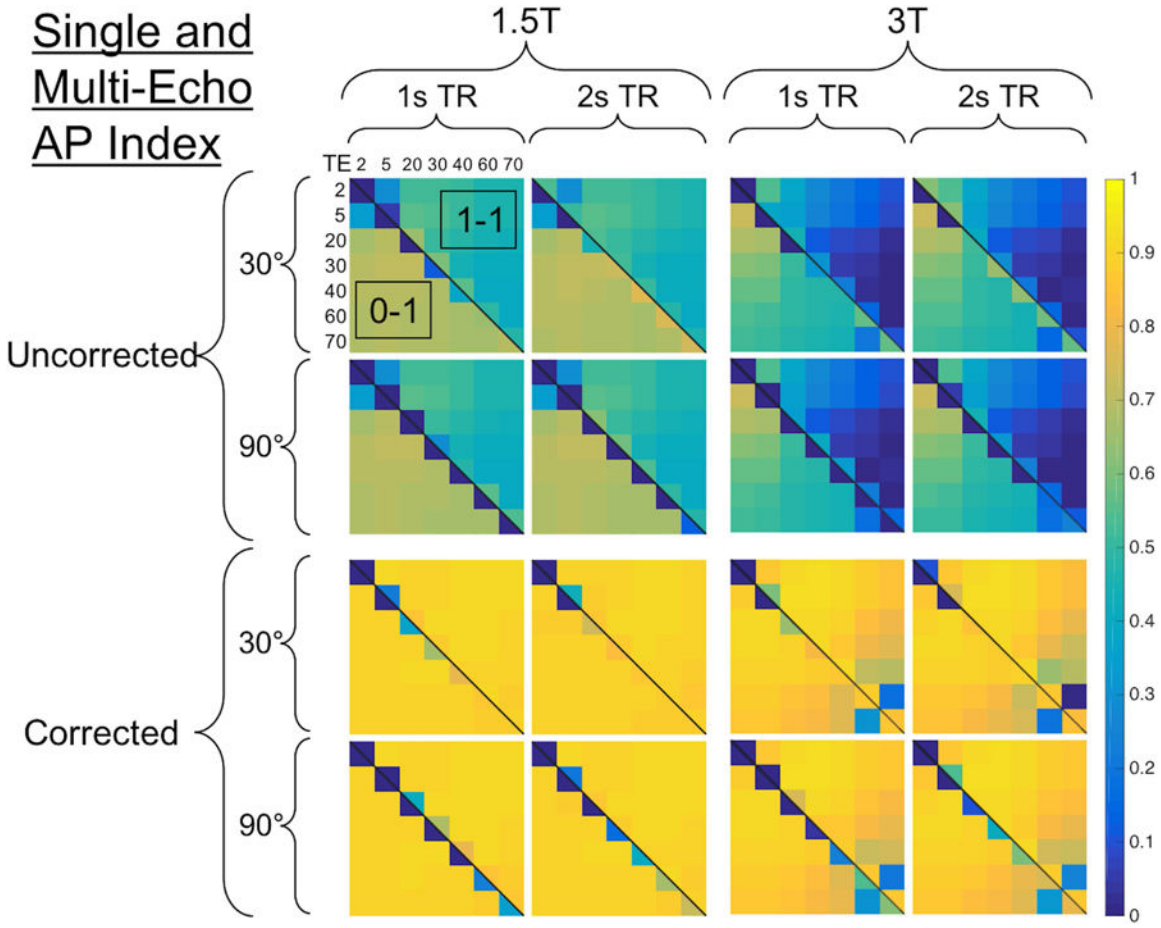


**Figure 7.**

CBV heat map showing the combined AP index across 896 parameter combinations (excluding 1.5s TR and 60 FA). The heat map is segmented vertically in half by field strength (left is 1.5T, right is 3T) and horizontally in half by leakage correction (top is uncorrected, bottom is BSW-corrected). For each field strength and leakage correction choice, the heat map is further segmenting according to TR (vertically for 1 and 2s TR) and FA (horizontally for 30 and 90º). Within each partition, the lower diagonal represents no preload ([0–1]), while the upper diagonal indicates with preload ([1–1]). The TEs are represented both horizontally and vertically, where the diagonal elements represent single-echo protocols for each TE and the off-diagonal elements represent each multi-echo TE combination (the multi-echo fit was excluded for brevity). Note the single-echo combinations along the diagonal are split according to preload doses. Higher accuracy is indicated by AP values closer to 1.

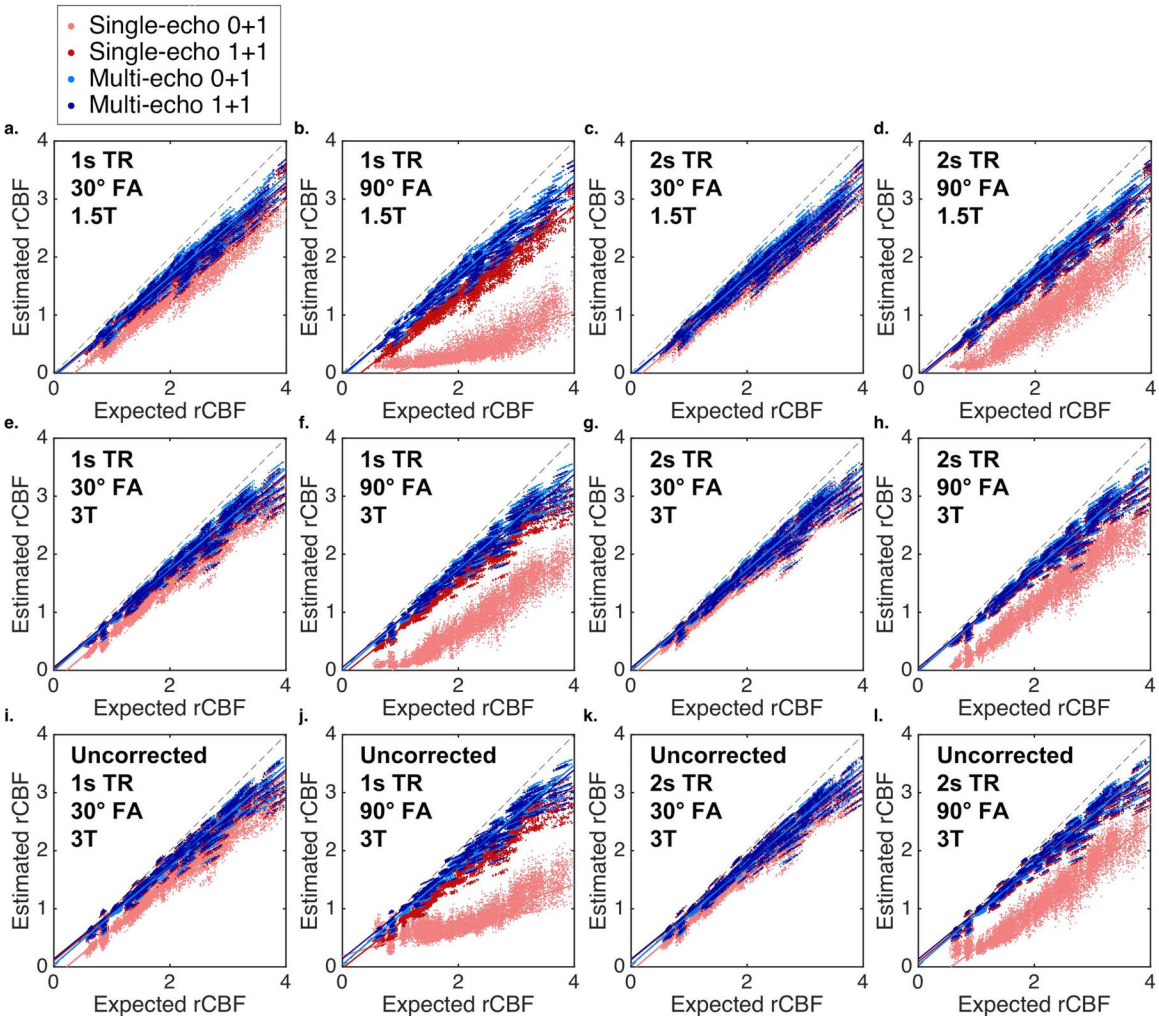


**Figure 8.**

Scatter plots between the expected (no leakage) and estimated (BSW-corrected) rCBF for single-echo (TE = 30ms, red) and multi-echo (TE = 2 and 30ms, blue) with no preload (light color) and with preload (dark color) for TR and FA combinations (columns) at 1.5 (a-d) and 3T (e-h). To determine the impact of leakage correction, the bottom row (i-l) shows uncorrected rCBF for each combination (3T only). Across all combinations, including both multi-echo and single-echo, there is a trend of increasingly underestimated rCBF as rCBF increases. Solid lines indicate best-fit lines, while the black dashed lines indicate the line of unity.

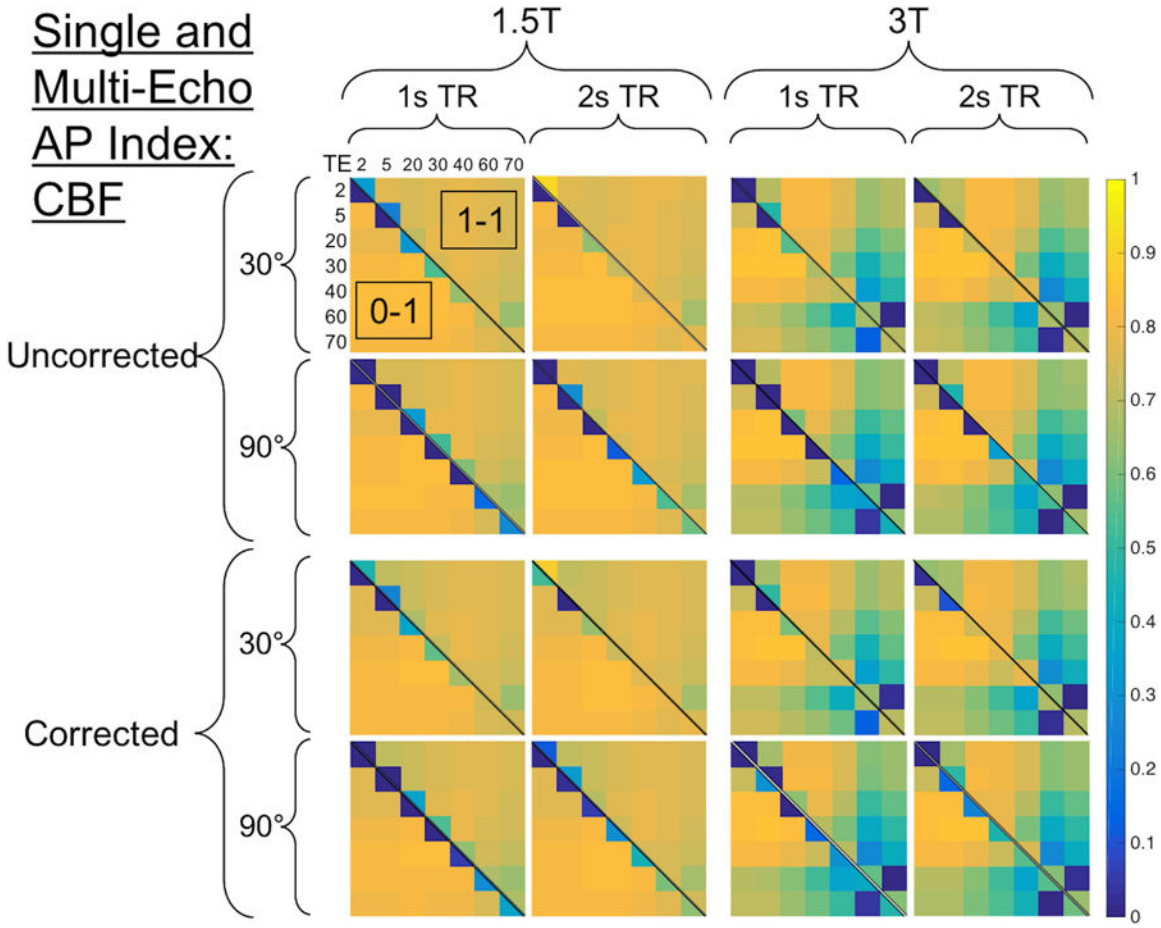


**Figure 9.**

CBF heat map showing the combined AP index across 896 parameter combinations (excluding 1.5s TR and 60 FA). See Figure 7 caption for heat map description.

**Table 1 –**

CCC, CV, and AP index for the top- and median-performing acquisition parameter combinations for both single-echo and multi-echo DSC protocols at each field strength and dosing scheme.

| | **Single-Echo Top-Performing** | | | | **Single-Echo Median AP Index** | | | | **Multi-Echo Top-Performing** | | | | **Multi-Echo Median AP Index** | | | |
|---|---|---|---|---|---|---|---|---|---|---|---|---|---|---|---|---|
| **Field Strength** | 1.5T | | 3T | | 1.5T | | 3T | | 1.5T | | 3T | | 1.5T | | 3T | |
| **Dosing Scheme** | [0+1] | [1+1] | [0+1] | [1+1] | [0+1] | [1+1] | [0+1] | [1+1] | [0+1] | [1+1] | [0+1] | [1+1] | [0+1] | [1+1] | [0+1] | [1+1] |
| **Protocol**<br>TE (ms)<br>FA<br>TR (s) | 70<br>60°<br>2s | | 30<br>30°<br>1.5s | | 40<br>60°<br>1s | 20<br>30°<br>2s | 40<br>60°<br>1s | 60<br>90°<br>1s | 30, 40<br>60°<br>1s | | 2, 30<br>60°<br>1s | | 40, 60<br>90°<br>2s | 20, 70<br>90°<br>1s | 5, 60<br>30°<br>2s | 30, 40<br>90°<br>1 s |
| **CCC** | 0.93 | 0.97 | 0.94 | 0.98 | 0.39 | 0.95 | 0.63 | 0.96 | 0.98 | 0.98 | 0.98 | 0.99 | 0.98 | 0.98 | 0.97 | 0.97 |
| **CV (%)** | 7.8 | 6.9 | 7.1 | 6.3 | 14.2 | 8.6 | 9.3 | 8.9 | 7.2 | 6.4 | 7.2 | 6.2 | 7.7 | 7.0 | 9.2 | 9.6 |
| **AP** | 0.85 | 0.91 | 0.87 | 0.92 | 0.25 | 0.87 | 0.54 | 0.87 | 0.91 | 0.92 | 0.91 | 0.92 | 0.90 | 0.91 | 0.88 | 0.87 |